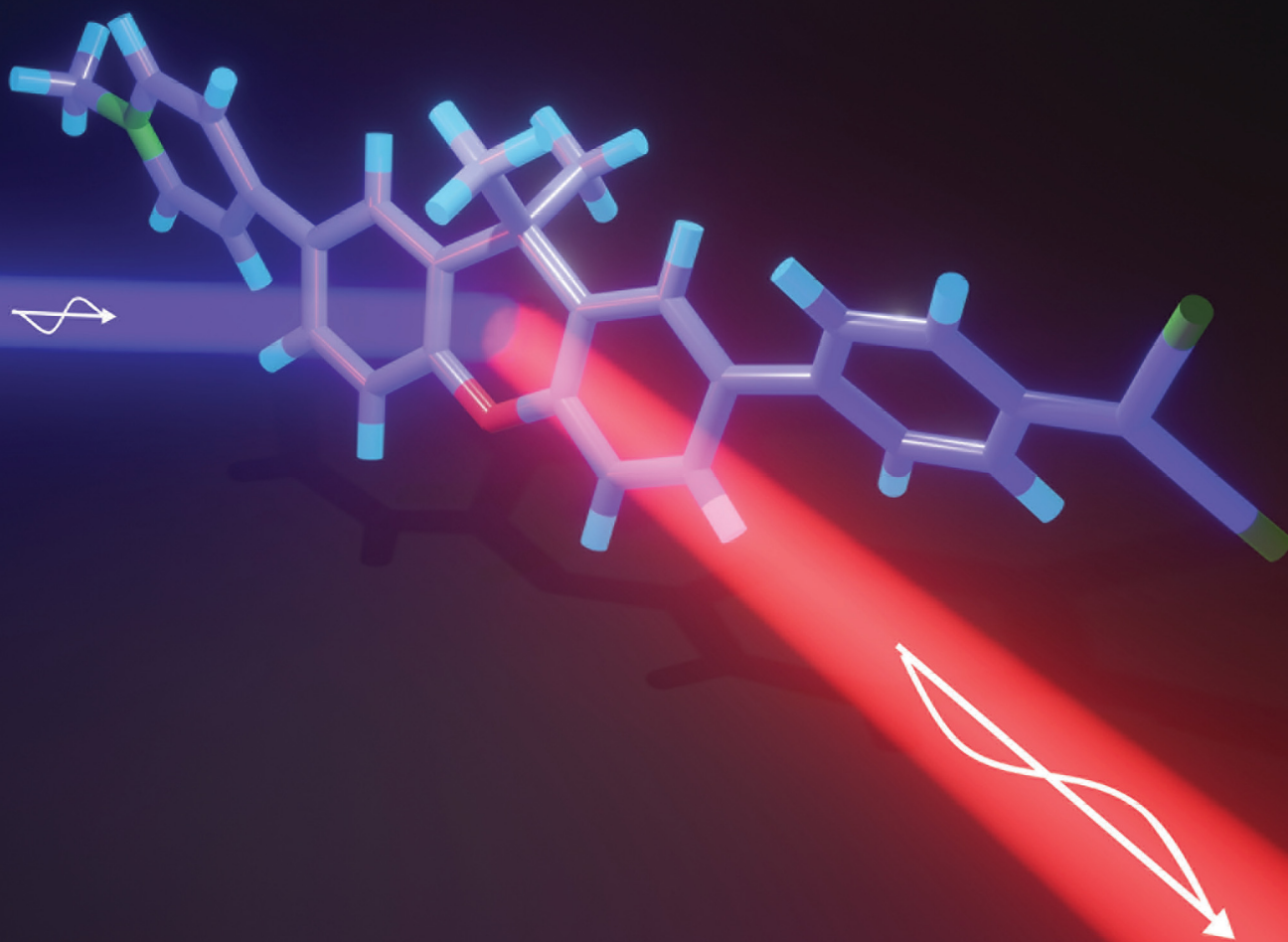


Materials Advances

Volume 3
Number 20
21 October 2022
Pages 7373–7676

rsc.li/materials-advances



ISSN 2633-5409

PAPER

Kaitlyn E. Crawford *et al.*
Modular synthesis of zwitterionic, xanthene bridged, low
twist angle chromophores with high hyperpolarizability

Cite this: *Mater. Adv.*, 2022, **3**, 7520

Modular synthesis of zwitterionic, xanthene bridged, low twist angle chromophores with high hyperpolarizability†

Gavin S. Mohammad-Pour,^{id} ab Yovan de Coene,^{id} c Meryl Wiratmo,^{id} ab
Aditya Maan,^{id} ab Koen Clays,^{id} c Artëm E. Masunov,^{id} defgh and
Kaitlyn E. Crawford^{id} *abde

Push–pull chromophores exhibit useful electro-optic (EO) properties that have the potential to significantly improve non-linear EO applications ranging from telecommunications to quantum informatics. Compounds with large hyperpolarizability values (β) that are stable and have easily modifiable functional groups are needed to advance organic-based EO systems. In this report, theoretical and experimental methods were used to investigate the design, synthesis, and application of a new class of push–pull chromophores for their use as a guest in guest–host EO polymer composites intended for non-linear EO applications. The chromophores combine the known intramolecular charge transfer benefits of increasing electron localization among π -conjugated zwitterionic structures with the aim of enhancing their β without the necessity of large dihedral angles. The class of chromophores reported here include a xanthene unit between a dicyanomethanide donor and pyridinium acceptor. This arrangement increases charge separation due to the central sp^3 hybridization and enables modular aliphatic substitutions while maintaining concise, high yielding synthetic steps. Chromophore design selection was guided by high-throughput quantum chemical Density Functional Theory calculations to predict β and dipole moment (μ) *a priori*. Out of 230 molecular candidates considered, we present the results for three chromophores: dicyano(9,9-dibutyl-7-(1-(2-ethylhexyl)pyridin-1-ium-4-yl)-9H-xanthen-2-yl)methanide (**E1**), dicyano(4-(9,9-dibutyl-7-(1-(2-ethylhexyl)pyridine-1-ium-4-yl)-9H-xanthen-2-yl)methanide (**E2a**), and (4-(9,9-bis(2-ethylhexyl)-7-(1-(2-ethylhexyl)pyridine-1-ium-4-yl)-9H-xanthen-2-yl)phenyl)dicyanomethanide (**E2b**). While bulk EO coefficients were low ($<2 \text{ pm V}^{-1}$), perhaps due to strong aggregation, the results demonstrate exceptional experimental Hyper Raleigh Scattering (HRS) β values. **Eb2**, for example has an HRS β value of $1650 \pm 150 \times 10^{-30}$ esu at 900 nm in acetonitrile, which corresponds to $\mu\beta$ of $86\,000 \times 10^{-48}$ esu and a $\mu\beta/M_w$ figure of merit (FOM) of 121×10^{-48} esu, where μ is the calculated dipole moment and M_w is the chromophore's molecular weight. The chromophores are moderately stable in ambient conditions, their size and shape are easily modifiable, and they exhibit strong negative solvatochromism with solvent polarity.

Received 21st June 2022,
Accepted 9th August 2022

DOI: 10.1039/d2ma00721e

rsc.li/materials-advances

^a Department of Materials Science and Engineering, University of Central Florida, Orlando, Florida 32826, USA. E-mail: kcrawford@ucf.edu

^b Biionix Cluster, University of Central Florida, Orlando, Florida 32827, USA

^c Department of Chemistry, KU Leuven, Celestijnenlaan 200D, 3001 Leuven, Belgium

^d Department of Chemistry, University of Central Florida, Orlando, Florida 32816, USA

^e NanoScience Technology Center, University of Central Florida, Orlando, Florida 32826, USA

^f School of Modeling, Simulation & Training, University of Central Florida, Orlando, Florida, 32826, USA

^g South Ural State University, Lenin pr. 76, Chelyabinsk 454080, Russia

^h National Research Nuclear University MEPhI (Moscow Engineering Physics Institute), Kashirskoye shosse 31, Moscow, 115409, Russia

† Electronic supplementary information (ESI) available: The following files are available free of charge: Synthetic details, NMR, TGA, UV-vis, DSC, CV, FTIR-ATR (PDF). See DOI: <https://doi.org/10.1039/d2ma00721e>

Introduction

Organic electro-optic (EO) materials have the potential to greatly improve our ability to modulate optical signals in comparison to traditional inorganic EO materials (e.g., LiNbO_3).^{1–3} Precise, on-demand manipulation of optical signals is critical for advancing technologies such as imaging,⁴ spectroscopy,⁵ photovoltaics,⁶ telecommunication,⁷ and quantum computing.⁸ Researchers are thus dedicating significant effort to the design and realization of organic EO materials that are stable, programmable and exhibit exceedingly large EO responses.

Push–pull molecules such as chromophores have been the focus of extensive study over the past few decades to identify



structures capable of achieving large first hyperpolarizability, β . Recently, π -conjugated zwitterions encompassing twist structures have emerged with unprecedented $\mu\beta$, a scalar product wherein β is vectorial hyperpolarizability and μ is the structure's dipole moment. Within these structures, strong intramolecular charge transfer occurs when transitioning from the ground state to the first excited state, while maintaining a large polarity along the π -conjugated axis – a driving force of traditional planar push-pull molecules. The structure's composition and the extent of its out-of-plane character facilitates twisted intramolecular charge transfer, TICT. By harnessing TICT chromophores, experimental $\mu\beta$ values up to $-488\,000 \pm 48\,000 \times 10^{-48}$ esu by Electric Field-Induced Second Harmonic Generation (EFISH) at 1907 nm in dichloromethane (CH_2Cl_2) has so far been reported.⁹ A caveat with EFISH is that μ and β cannot be measured independently, which leaves some ambiguity in their precise, individual values. For $\mu\beta$ comparison using the same experimental conditions for common planar, donor-acceptor chromophores, disperse red 1 (DR1) is 480×10^{-48} esu; and FTC-1 is $17\,600 \times 10^{-48}$ esu, Chart 1.^{10–12} In the latter case, β was also measured independently to be 635×10^{-30} esu by Hyper Rayleigh Scattering (HRS).¹² When the FTC-1's β from HRS is paired with its computed μ , then the combined $\mu\beta$ is 8550×10^{-48} esu. In considering other common planar, donor-acceptor chromophores, JRD1 and HLD1, their β from HRS at 1300 nm are $3300 \pm 50 \times 10^{-30}$ esu and $2120 \pm 50 \times 10^{-30}$ esu, respectively.¹³ Although the examples provide a relative comparison, caution is to be exercised because reported values are often collected under different experimental conditions (*e.g.*, measurement wavelength and solvent choice).

Despite large $\mu\beta$ reported by EFISH, TICT π -conjugated zwitterions tend to exhibit lower than expected EO response (measured as the EO coefficient r_{33}) in EO polymer composites, likely because of their propensity to aggregate. Their synthesis can also be laborious. However, there remains much to discover in developing zwitterionic TICT chromophores as they are a relatively new class of push-pull structures.⁹ The first theoretical prediction that TICT chromophores could potentially

exhibit unprecedented hyperpolarizabilities was published in 1997 and based on tetraalkyl-substituted 4-quinopyran, abbreviated TICTOID (and TM-1), Chart 1. In this example, the interplanar dihedral angle was 104° and $\mu\beta$ was $\sim 70\,000 \times 10^{-48}$ esu at an excitation energy of 0.10 eV.^{14,15} In comparison, the unsubstituted, planar counterpart yielded theoretical $\mu\beta$ of 27.9×10^{-48} esu.¹⁵ The first experimental TICT example followed in 2005 based on two zwitterionic compounds with tetra-*ortho*-alkylbiaryl cores, a dicyanomethanide electron donor, and a pyridinium electron acceptor, abbreviated as TMC-2 and TMC-3. The composites feature $\mu\beta$ values up to $-488\,000 \times 10^{-48} \pm 48\,000 \times 10^{-48}$ esu, characterized by EFISH, Chart 1.¹⁶ In this example, the Teng Man method was additionally used to demonstrate experimental r_{33} EO coefficients at 1310 nm with 10% TMC-2 and 5% TMC-3 in poly(vinyl phenol) as individual electro optic polymer (EOP) composites. These combinations resulted in 48 pm V^{-1} and 320 pm V^{-1} only while poling, respectively (compare with $\sim 31 \text{ pm V}^{-1}$ for inorganic counterpart, LiNbO_3). Poly(vinyl phenol) was used instead of other traditional polymer hosts such as polycarbonate or polymethyl methacrylate, because of the significantly attenuated r_{33} in those polymers. Further, typical concentrations for freely mixed chromophores in an EO polymer matrix range from 20% to 30%.¹⁷ However, doping levels for π -conjugated zwitterionic chromophores can be limited due to strong intermolecular interactions¹⁸ and likely explains the use of lower concentrations. Since the first TICT experimental debut, several other reports of π -conjugated zwitterionic TICT chromophores have emerged.^{19–27} Although they were generally tedious to synthesize, these chromophores hold the theoretical $\mu\beta$ record of $820\,000 \times 10^{-48}$ esu, according to INDO/SCI calculations for 4TTMC, a TMC derivative with 4 aryl linkages. In this example, 4TTMC features three twist angle locations ranging from 40.3° to 88.42° , Chart 1.^{9,11} Experimental characterization of $\mu\beta$ was not possible¹¹ and the r_{33} was not reported. Instead, 2TTMC, a TMC derivative with 2 aryl linkages and a twist angle of 67° , exhibits $\mu\beta$ of $-6\,000 \times 10^{-48}$ esu measured by EFISH in CH_2Cl_2 at 1907 nm, as compared to $\sim 12\,000 \times 10^{-48}$ esu computed using INDO/SCI.⁹ Collectively, these and similar critical, foundational studies^{19–27} demonstrate

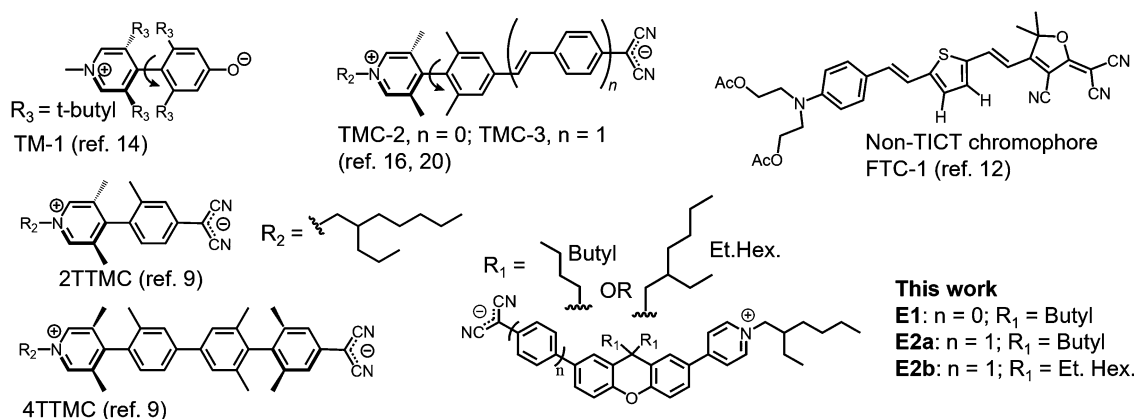


Chart 1 Example TICT chromophore structures and non-TICT: FTC-1.



that π -conjugated zwitterionic TICT chromophores have potential to significantly increase experimental $\mu\beta$, which could eventually translate to exceptionally large EO coefficients well beyond values observed in traditional, non-TICT, donor-acceptor chromophores (see Liu *et al.* for a review on traditional chromophores).⁸ First however, there is a need to develop π -conjugated zwitterionic TICT chromophores with sites available for modular side-group functionalization to mitigate aggregation and achieve high product yields. $\mu\beta$ and β values are tabulated for different TICT and non-TICT chromophores in Table S1 (ESI†).

In this study, we use a combination of computation and experiment to identify a class of zwitterionic TICT chromophores with large $\mu\beta$. The chromophores consist of a xanthene bridge with dicyanomethanide donor and pyridinium acceptor moieties. While each of the individual components (*i.e.*, bridge, donor, acceptor) are well known,^{28–30} the unique combination of the donor/acceptor with the xanthene bridge has never been reported. Our selection of xanthene as a bridge to synthesize new TICT chromophores was intentional because it (1) would likely enhance charge separation between the donor/acceptor and promote their out of plane rotation due to xanthene's size and planar structure, and (2) is easily modifiable toward the formation chromophores with variable size and shape for future use in non-linear optic applications. We show that these chromophores are capable of modular side-group functionalization through straightforward synthetic techniques. We demonstrate synthetic feasibility of the new chromophores and their side group interchangeability; compare their calculated *vs.* experimental $\mu\beta$; then evaluate and discuss their structural, chemical, and optical properties. We use Density Functional Theory (DFT) to calculate μ and β of the new chromophores. Spectroscopy techniques, NMR, ATR-FTIR and LC-MS, confirm the intermediate and final product structures. DSC and TGA provide information on their thermal properties. HRS, UV-vis, cyclic voltammetry, and the Teng Man method enable visualization of their optical and electronic properties. The results demonstrate exceptional experimental HRS β values as high as $1650 \pm 150 \times 10^{-30}$ esu at 900 nm in MeCN. This β value corresponds to $\mu\beta$ of $86\,000 \times 10^{-48}$ esu when combined with calculated μ , and $\mu\beta/M_w$ figure of merit (FOM) of 121×10^{-48} esu, where M_w is the molecular weight of the chromophore. The following includes a discussion on the similarity and differences of the structures and experimental parameters leading to the observed $\mu\beta$ values.

Experimental

Materials and methods

Reagents. All starting materials and solvents were obtained from commercial sources (Aldrich, Fisher, VWR) and were used without further purification unless otherwise specified. 1-Iodopyridine,³¹ tetramethyl-2-[4-(trimethylsilyl)phenyl]-1,3,2-dioxaborolane,³² 9,9-dibutyl-9H-xanthene,³³ and 2-ethylhexyl triflate⁹ were synthesized according to literature procedures. Tetrahydrofuran (THF), *N,N*-dimethylformamide (DMF), MeCN

and CH_2Cl_2 were purified using a solvent purification system (Innovative Technology) with custom-built alumina columns. 1,2-Dichloroethane (DCE), chlorobenzene (PhCl) and chloroform (CHCl_3) were dried using 4 Å molecular sieves.

Spectroscopic analysis. Nuclear Magnetic Resonance (NMR): ^1H , ^{13}C , ^{19}F , and HMBC NMR spectra were collected using a Bruker AVANCE-III 400 MHz spectrometer. Tetramethylsilane (TMS) at 0 ppm and C_6F_6 were used as internal standards to assign chemical shifts for ^1H and ^{13}C , and ^{19}F , respectively. Infrared Attenuated Total Reflectance spectroscopy (FTIR-ATR): Infrared spectra were collected on a JASCO 6600. Liquid Chromatography-Mass Spectrometry (LC-MS): High resolution mass spectra were recorded using an Agilent 6230 TOF coupled with an Agilent Zorbax SB-C18 analytical column. Ultraviolet-Visible-Near-Infrared Absorbance Spectroscopy (UV-vis): Absorbance measurements were out carried under ambient conditions on a Horiba Duetta spectrometer with wavelengths between 300–800 nm. Molar absorptivity for chromophores **E1** and **E2a–b** were obtained using a 3 to 5-point calibration curve within the limit of linear detection for the reported wavelength. For chromophore-solvent combinations where the spectrum shifts with concentration, the 3 highest concentrations were used as these resulted in the least deviation between samples. Chromophore **E1** and **E2b** were analyzed across 8 dry solvents: MeCN, DMF, acetone, CHCl_3 , THF, PhCl, CH_2Cl_2 , and DCE. Chromophore **E2a** was analyzed across 3 dry solvents due to limited solubility: MeCN, DMF, and acetone.

Thermal and stability analysis. Thermogravimetric Analysis (TGA) was conducted using a Shimadzu TGA-50 apparatus with temperature range between 25 °C and 800 °C. Differential Scanning Calorimetry (DSC) was conducted using a Netzsch Polyma 300 calorimeter with 20 °C min^{-1} heating and cooling rates. Samples were prepared by hermetically sealing ~8 mg of product in aluminum pans. Curves of the second heat and first cool were recorded. The melting temperature of neat chromophores were determined using a Melt-Temp brand Electrothermal 1101D melting point apparatus measured by a Fluke II Digital Thermometer. Air and moisture stability were evaluated by collecting ^1H NMR spectra of ~2 mg of chromophore dissolved in $\text{DMSO-}d_6$ under ambient conditions (room temperature and 55% humidity) at 1 h, 24 h, and 72 h.

Electrochemical analysis. Cyclic voltammetry (CV) was performed in an Ar-filled glovebox with a 730C SI Instruments biopotentiostat-galvanostat at a 100 mV s^{-1} scan rate. Analyte solutions were prepared at a 1.0 mM chromophore concentration in 0.1 M (tetrabutylammonium)PF₆/MeCN electrolyte with a 2 mm Pt-disc working electrode, and Pt counter and reference electrodes. Potential was referenced against ferrocene ($\text{FcCp}_2^+/\text{FcCp}_2$) at 0 V as an internal standard.

Poling and electro optic coefficient (r_{33}). The electro-optic coefficient was measured by Nonlinear Materials Corp. using the ellipsometric technique under ambient conditions. All samples were prepared in cleanroom and inert atmosphere environments prior to poling and r_{33} measurement according to the following procedures: 10 wt% **E1** and 5 wt% **E2a**, each with 15 wt% amorphous poly(vinyl phenol) in DMF were



prepared. The solutions were spun cast on ITO-glass slides with a sequential spin recipe of 500 rpm for 5 s, 850 rpm for 30 s and 1200 rpm for 30 s, each with 500 rpm s^{-1} acceleration. Film thicknesses were characterized by an NT-2000 model profilometer (WYKO Corp.). Refractive index (n) and extinction coefficient (k) values were measured by variable angle spectroscopic ellipsometry (VASE) analysis of chromophore thin films on glass substrates using a J. A. Woollam M-2000 ellipsometer. The films were coated with Au (60 nm) as top electrode *via* electron beam evaporation. Samples were poled under nitrogen at 25 V μm^{-1} and 110 $^{\circ}\text{C} \times 5$ min.

Hyper rayleigh scattering (HRS). Measurements were performed with a 900 nm fundamental wavelength from a mode-locked femtosecond laser source (~ 1 W_{ave}, 80 MHz, Spectra-Physics, Insight DS+) with a spectrally resolved detection (90 $^{\circ}$, Bruker IS/SM 500 spectrometer, Andor Solis iXon Ultra 897 EMCCD camera). The spectrally resolved total signal (including the narrow HRS peak and any broad multiphoton fluorescence bands) were fitted to a sum of Gaussian bands. MeCN (anhydrous, 99.8%, Aldrich) was assigned a static $\beta_{0,ZZZ}$ value of 0.578 $\times 10^{-30}$ esu based on work by Campo *et al.*³⁴ Details of the experimental set-up and data analysis are published.³⁵

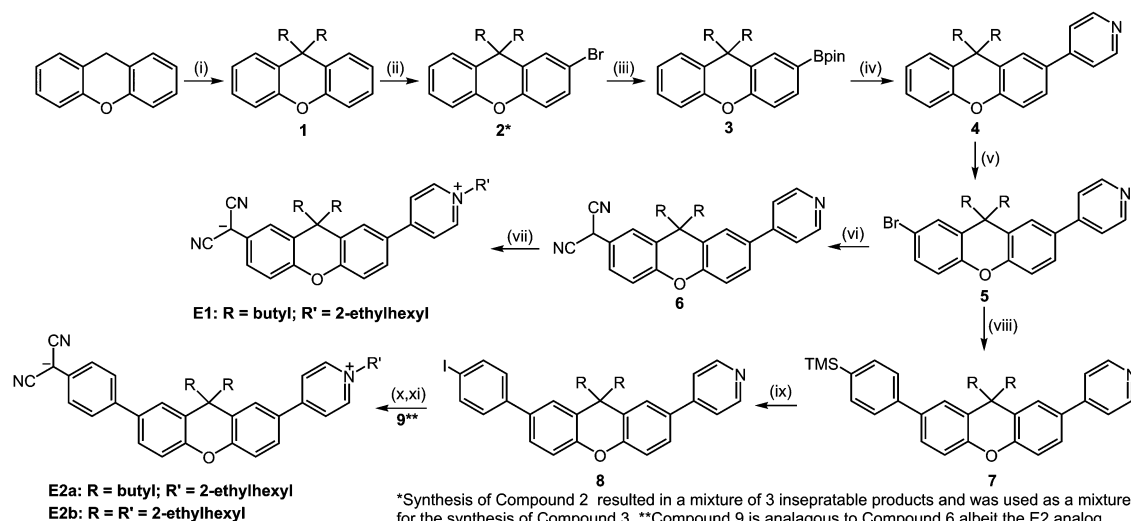
Computations. All quantum chemical calculations were performed using *Gaussian 16* suite of programs³⁶ at the DFT level in conjunction with D95+* basis set.³⁷ Molecular geometry optimization and hyperpolarizability predictions were performed using M06-2X exchange-correlation functional. According to a recent report,³⁸ M06-2X functional provided superior predictions of relative β_{HRS} values but poorer predictions of λ_{max} . Therefore, the absorption spectra were predicted by finding 24 excited states with Time-Dependent DFT (TDDFT) approach, where the solvent effects were accounted for by using the dielectric continuum model in the solvent model density (SMD) parameterization,³⁹ as implemented in Gaussian 16. The M05-QX exchange-correlation functional was derived⁴⁰ by interpolation between M05 and M05-2X functionals.⁴¹ M05-QX

includes 35% of the exact exchange and was shown to closely predict the energies not only for the lowest, but for the higher-laying excited electronic states as well. A reliable estimation of hyperpolarizability typically requires wavefunction theory levels that include electron correlation (such as coupled cluster methods, *etc.*), while DFT with the commonly used B3LYP functional tends to overestimate hyperpolarizability values.⁴² Improvements at the DFT level, however, can be accomplished by increasing the fraction of Hartree-Fock (HF) exchange in hybrid exchange-correlation functional.⁴³⁻⁴⁶ When predicting other nonlinear optical properties, such as two-photon absorption (2PA) cross-sections, the optimal results can be achieved when M05-QX functional with 35% HF exchange is used.⁴⁷⁻⁵⁰ However, increase in fraction of HF exchange beyond 42% was shown to be disastrous: it leads to significantly overestimated state energies and underestimated transition dipoles.⁵¹ The reason for superior performance of M05-QX functional is likely to be related to more accurate description of the contribution of charge transfer into electronically excited states. This is evidenced by the comparing values of the dipole moments obtained with coupled cluster methods *vs.* the ones obtained with M05-QX functional.⁵²

Results and discussion

Synthesis

Synthetic paths to chromophores **E1**, **E2a**, & **E2b** is in Scheme 1. Mediated by an *in situ* formed base resulting from the reaction between DMSO and sodium hydride, the synthesis of compound **1** was achieved *via* a nucleophilic substitution of 1-iodobutane at the 9-position of xanthene. Attempts to use alternative methods of xanthene deprotonation were unsuccessful or resulted in the formation of a mono-9*H*-substituted xanthene. While butyl and 2-ethylhexyl aliphatic groups were used for the compounds illustrated here, this substitution step is important as it highlights one of the first places that the



Scheme 1 Synthetic pathway for **E1** and **E2a-b**.



xanthene-class chromophores can be variably customized. Exchanging the aliphatic substituents for one of many different isolation groups requires only the addition of a sufficiently reactive electrophile.

To progress to compound **2**, sequential bromination of the xanthene core must be achieved. As it was not possible to substitute only one side without the formation of some dibrominated xanthene, nor was it possible to separate the products *via* column chromatography, this product was used as a mixture in the following step. The formation of the boronate ester, compound **3**, is achieved by a standard *n*-butyl lithium borylation of the compound **2** mixture and 2-isopropoxy-4,4,5,5-tetramethyl-1,3,3-dioxaborolane, with a slight excess of both reagents used to account for the amount of di substituted product present. It is at this step where the mixture was purified *via* column chromatography using 2.5% ethyl acetate (EtOAc) in hexanes, with extra care given to minimizing the contact time between the boronate product and silica to avoid boronate deprotection.

The central xanthene moiety was to be first coupled with a *p*-halogenated pyridine compound, beginning the formation of what would eventually become the electron acceptor of our chromophores. First, it should be noted by those who are not familiar with *p*-halogenated pyridines, that they are highly unstable, even when stored at low temperatures. This instability increases moving up the halogen column of the periodic table resulting in 4-iodopyridine being the easiest to work with. Freshly prepared iodopyridine that appears white, or at the very least yellow, will perform adequately as a Suzuki coupling partner, however if the iodopyridine has been stored for some time (*e.g.*, a week or longer), the formation of dark spots signifies the formation of a problematic degradation product. This product, if not removed *via* physical separation (*i.e.* manually separating the dark spots with a spatula) or sublimation, will poison the Pd-catalyst upon heating *via* an unknown mechanism. It is worth noting that the low steric hindrances between aromatic groups of this system affords a synthetic advantage in that it does not require the application of specialty Pd-ligands and can be performed with the generic Pd(PPh₃)₄ with moderately high yields (87%).

Starting with compound **4** and ending with compounds **5** and **9** (for **E1** and **E2a-b**, respectively), is where some initial difficulties in the overall synthetic scheme arose. The chemical modifications between these intermediates have such similar polarities that they cannot be easily distinguished or separated by common chromatographic techniques, specifically thin-layer and column chromatography. Column separations were run with automated columns for which the solvent ratios are provided in the ESI.† They yield differences in apparent fluorescence, which can indicate that the reaction is progressing, but the nearly identical retention factors between these intermediates cannot yield an understanding of the degree to which the reactions have progressed. This fact was certainly limiting during the optimization process as many times the reactions were either not heated to high enough temperatures, taken off heat too early, or without sufficient reagent equivalents. There

are alternative routes that do not have this limitation, and indeed the works that inspired our research, understandably, follow this approach.⁹ However, post-optimization, we found that the higher yields, ease of setup/workup, and decreased synthetic steps justified our method.

The bromination of the second xanthene position, used to attach what would be the donor portion of the chromophore, is surprisingly dissimilar in reactivity from the first bromination step. For the bromination to progress at a moderate pace the amount of NBS needed to be increased to two equivalents and then heated to 80 °C for at least 12 hours, yielding compound **5** (75% yield). Next, the synthetic path is divergent between performing a Pd-catalyzed malononitrile coupling leading to compound **6** (65% yield) and subsequently **E1** (55%), and progressing *via* Suzuki coupling to compound **7**, and eventually leading to chromophore **E2a**. The Suzuki coupling to form compound **7** was carried out in a DME/EtOH solvent system with K₂CO₃ and Pd(PPh₃)₄. We found that a solvent system excluding water resulted in an elimination of the desilylation process with a yield of 79% for compound **7**. The subsequent formation of the aromatic iodide, compound **8**, was easily achieved using a simple ICl and CH₂Cl₂ iodination reaction (89% yield).

The next steps involve the Pd-catalyzed aryl-malononitrile coupling, which yield compounds **6** (65% yield) and **9** (59% yield) for chromophores **E1** and **E2a** respectively. In both cases when the reaction is quenched the pH of the aqueous phase must be neutralized to avoid yield losses from either the basic or acidic forms of these compounds. Finally, the synthesis concludes in a two-step, one-pot nucleophilic substitution of the pyridine on a aliphatic 2-ethylhexyl triflate, followed by deprotonation of the dicyanomethine group with sodium ethoxide. Given the high solubilities of **E1** and **E2b**, both were purified *via* column chromatography in 5% MeOH:CH₂Cl₂, resulting in yields of 55% and 78%, respectively. Pure **E2a** was obtained by washing with solvents resulting in a 73% yield.

Molecular structure

NMR, IR, and LC-MS characterization confirm the molecular structures for each synthesized compound, including the resulting chromophores **E1** and **E2a-b** (see ESI†). The incorporation of three racemic 2-ethylhexyl groups, as found in **E2b**, causes a complex array of signals in the aromatic region because it is a diastereomeric mixture (Fig. S21, ESI†). Regardless, the total integration values of the aromatic region correspond to a total of 14 aromatic protons, with the combined pyridinium aromatic signals at 8.62 and 9.04 ppm, manifesting as signals that are discrete enough to act as the integration point of reference for the remaining resonances. The aliphatic regions for both **E1** and **E2a** are nearly identical and represent the overlapping signals of the two central butyl groups and the 2-ethylhexyl chain on the pyridinium with an expected combined integration of 35 protons. The aliphatic region for **E2b** has greater signal overlap accounting for the two central 2-ethylhexyl groups and the third 2-ethylhexyl chain on the pyridinium with an expected combined integration of *ca.* 51



protons. ^{13}C NMR spectra in Fig. S18 and S20 (ESI †) depict the appropriate number of signals expected for both compounds. **E2b**, however, is a diastereomeric mixture resulting from the 3 chiral centers, which yields too many peaks for accurate determination. The chemical structure for **E1** is further articulated by HMBC NMR, which confirms the donor–acceptor substitution pattern relative to the 2 and 7 positions on the xantheno (Fig. S23, ESI †). Each chromophore, as synthesized, contains a counterion for the pyridinium functional group in the form of a triflate, which is verified *via* ^{19}F NMR showing a chemical shift of -80.1 ppm for each of the chromophores. (Fig. S24–S26, ESI †) The ^{19}F NMR were collected post-column chromatography suggesting that some anion moved through the silica, likely as a close ion pair. Zwitterions can form counter ions coordination with the introduction of ionic liquids.⁵³

Structural stability

^1H NMR analysis provide details of the moisture, air, and thermal stability. Fig. 1 provides ^1H NMR spectra for **E1** and **E2a–b** upon exposure to air with ambient moisture over 72 h. The spectra indicate that while **E2a–b** are largely stable, **E1** shows significant degradation over 72 h. **E2a–b** eventually degrade over a much longer period (>1 week, not shown). This behavior is notably different from previous TICT chromophores where chemical stability decreases with increasing molecular length resulting from a stronger charge localization on the hygroscopic, nucleophilic dicyanomethanide.¹ **E1**'s lower stability likely stems from proximity of the dicyanomethanide carbanion to the electron donating properties of xantheno's central ethereal oxygen, which is a structural feature that is unique to this TICT class. That is, the electron donating properties of the xantheno bridge and its proximity to the dicyanomethanide makes it more basic and thus more likely to degrade compared to **E2a–b** in which the xantheno and dicyanomethanide are separated by a phenyl ring. When performing degradation studies under light and dark conditions we observed no discernible differences between the two conditions (not shown).

UV-vis analysis

Evaluating the optical properties of **E1** and **E2a–b** provides information about the electronic properties of these conjugated structures. Table 1 presents the λ_{max} and an estimation of the indirect bandgap for **E1** and **E2a–b** by determining the X-intercept from the peak shoulder of the longer wavelength. Fig. 2a depicts a hypsochromic shift in the visible spectrum with increasing solvent polarity for **E1**. Of the solvents investigated, CH_2Cl_2 exhibits the highest intramolecular charge transfer wavelength λ_{ICT} for **E1** at 593 nm, followed by DCE (583 nm), THF (569 nm), PhCl (559 nm), CHCl_3 (526 nm), acetone (517 nm), DMF (486 nm), and MeCN (476 nm) such that $\text{CH}_2\text{Cl}_2 > \text{DCE} > \text{THF} > \text{PhCl} > \text{CHCl}_3 > \text{acetone} > \text{DMF} > \text{MeCN}$ from 593 nm to 476 nm. The general negative solvatochromism trend suggests stabilization of the chromophore's ground state energy resulting in an increased HOMO–LUMO gap. Fig. 2b depicts the molar absorptivity values for the full UV-vis spectrum of **E1** in the same solvents except for CH_2Cl_2 , which was excluded because of the nonlinear correlation between absorbance and concentration over the range analyzed (1.0×10^{-4} M to 1.2×10^{-5} M); a difference we attribute to the breaking up of an aggregate structure. The λ_{max} values for **E1** emerge in the UV region between 374 nm and 341 nm. For the same chromophore, DCE exhibits the highest λ_{max} at 374 nm, followed by THF (369 nm), PhCl (367 nm), CH_2Cl_2 (365 nm), CHCl_3 (363 nm), acetone (350 nm), MeCN (344 nm), and DMF (341 nm) such that $\text{DCE} > \text{THF} > \text{PhCl} > \text{CH}_2\text{Cl}_2 > \text{CHCl}_3 > \text{acetone} > \text{MeCN} > \text{DMF}$. The small differences in peak trends between λ_{ICT} and λ_{max} as a function of solvent polarity are likely attributed to the complex nature of multiple overlapping peaks corresponding to the high energy electronic transitions of molecular subfragments.

In comparison to **E1**, chromophores **E2a** and **E2b** exhibit almost no spectral response in the visible region regardless of solvent or concentration choice and high levels of optical transparency in the near-IR (Fig. S27, ESI †). This observation manifests visually in solvent solutions that range in color from pale red to yellow. Fig. 2c and d show that any discernible visible absorbance bands are broad and are largely overshadowed by the

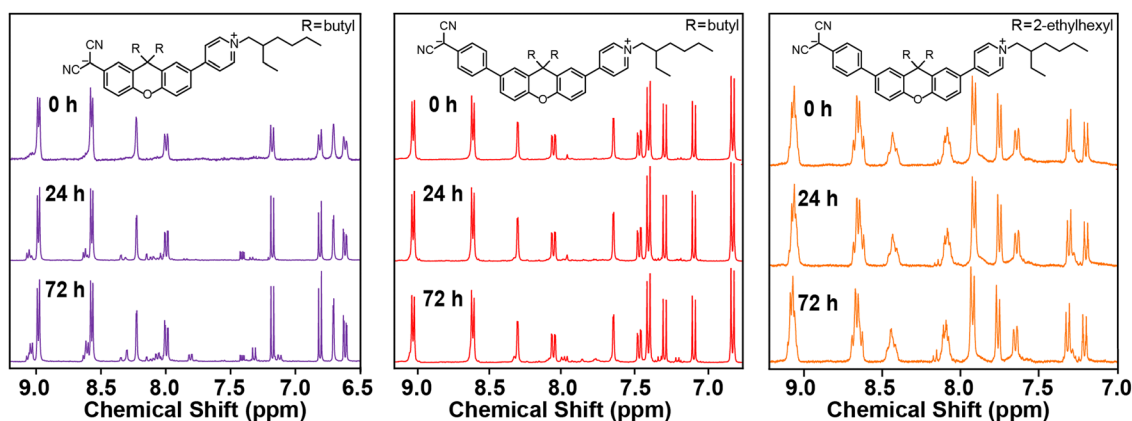
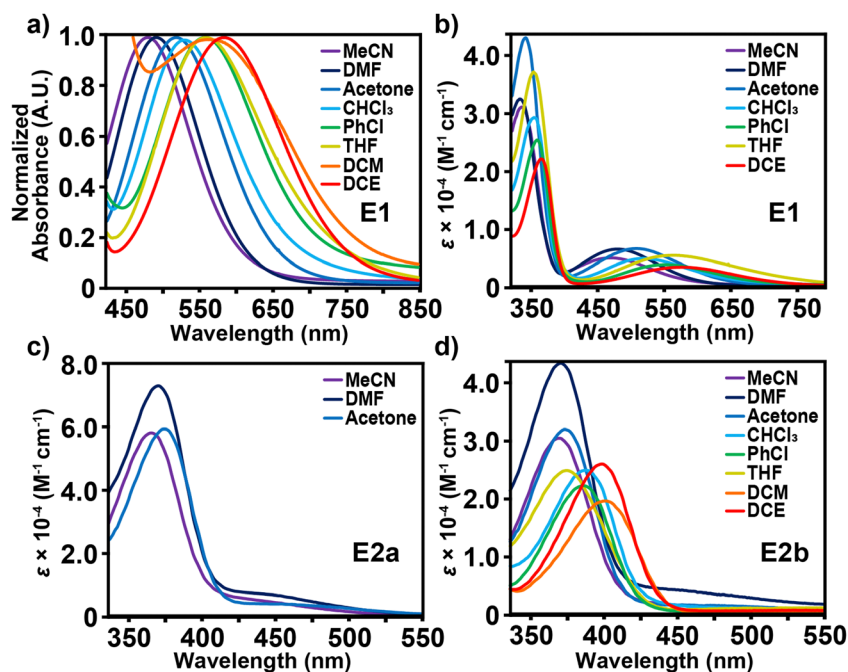


Fig. 1 Stability tests of chromophores dissolved in $\text{DMSO}-d_6$ under ambient conditions and measured at 0, 24, and 72 h.



Table 1 Computed dihedral twist angles, estimated band gap values, absorption properties, and temperature at 10% weight loss during TGA degradation for **E1** and **E2a-b**

Structure	Computed twist angle (degrees)		Band gap, ΔE (eV)			Absorption		TGA
	Bridge-accepter	Bridge-donor	Optical	E-Chem.	Computed	λ_{\max} (nm)	ϵ ($M^{-1} \text{ cm}^{-1}$)	10% Wt Loss ($^{\circ}\text{C}$)
E1	11.6	N/A	2.05	1.99	2.40	344	$31\,600 \pm 1600$	293
E2a	16.8	25.6	2.37	2.06	2.96	360	$58\,200 \pm 3400$	274
E2b	17.4	35.0	2.33	2.03	2.96	365	$30\,600 \pm 800$	360

**Fig. 2** (a) Normalized visible spectrum of chromophore **E1** in various solvents. (b–d) UV-vis molar absorptivity values in various solvents, averaged from 3–5 data sets within the linear range: (b) **E1** wherein CH_2Cl_2 is excluded due to the nonlinear ICT absorbance loss related to concentration; (c) **E2a** in only MeCN, DMF and acetone due to lack of solubility in the remaining solvents; (d) **E2b**.

peaks in the UV region, which are likely the λ_{ICT} for these compounds. Comparison between **E2a** and **E2b** is limited by the solubility of **E2a** in only MeCN, DMF, and acetone. Based on these 3 solvent comparisons **E2a** clearly has a much larger extinction coefficient in the UV region than **E2b** as well as λ_{ICT} bands that extend further into the visible region. The larger extinction coefficient is likely due to the effect of solvation from the highly branched and racemic combinations of the three chiral aliphatic chains on **E2b**. Interestingly, for **E2a** and **E2b** there is negligible shift in absorbance values as a function of concentration, which is an uncommon characteristic of zwitterionic dyes. On the other hand, **E1** exhibits a shift in wavelength and absorptivity as a function of concentration for THF, CHCl_3 , PhCl, and CH_2Cl_2 . The observable wavelength shifts are most prominent for THF and CHCl_3 , Fig. 3. When analyzed in concentrations ranging from $1.0 \times 10^{-4} \text{ M}$ to $1.2 \times 10^{-5} \text{ M}$, THF exhibits the largest λ_{ICT} absorbance shift of 556–577 nm accompanied by a slight decrease in molar absorptivity as well as an expansion of the UV bands' right shoulder. CHCl_3 shows no shift in wavelength with decreasing concentration but does exhibit a greater decrease in

absorptivity and a more prominent expansion of the right side of the UV band. Concentration-based spectral shifts for PhCl and CH_2Cl_2 may stem from in-solution aggregation as a function of concentration, Fig. S31 (ESI[†]).

Hyper rayleigh scattering (HRS)

The best fit experimental β_{ZZZ} values at 900 nm in MeCN for the present chromophores are **E1** = $(370 \pm 10) \times 10^{-30} \text{ esu}$, **E2a** = $(1520 \pm 80) \times 10^{-30} \text{ esu}$, and **E2b** = $(1650 \pm 150) \times 10^{-30} \text{ esu}$, Table 2. These values stem from the following guidelines: first, the HRS signal is taken as the total peak area in the nonlinear scattering spectrum corresponding to the narrow hyper-Rayleigh scattering at the second-harmonic wavelength of 450 nm. The peak signal results from the constant contribution from the solvent and a solute-concentration dependent contribution from the chromophores. Second, a Beer-Lambert correction factor is used for each chromophore because of the self-absorption of their generated photons at 450 nm. Third, with static $\beta_{0,\text{ZZZ}} = 0.578 \times 10^{-30} \text{ esu}$ as a reference for dry solvent³⁴ and by using an undamped two-level model,³⁷ the dynamic



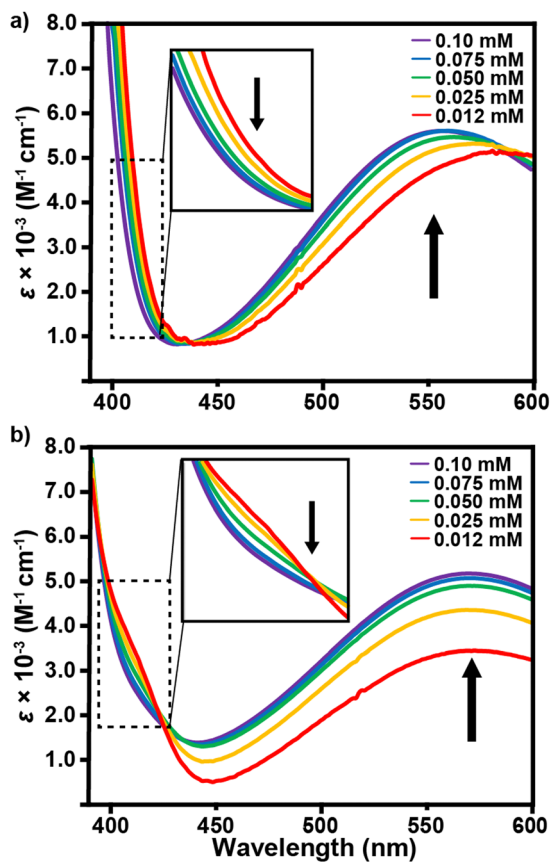


Fig. 3 Shifts in UV-vis molar absorptivities with as a function of concentration for chromophore **E1** in (a) THF and (b) CHCl_3 . Arrows denote directional correlation between absorptivity and concentration.

Table 2 μ and absolute $|\beta|$ values from calculation (static) and experiment (at 900 nm in MeCN)

Structure	Computed (M06-2x/D95 + * level)		HRS		
	μ (Debye)	$ \beta_{zzz} $ (10^{-30} esu)	$ \mu\beta_{zzz} $ (10^{-48} esu)	$ \beta_{zzz} $ (10^{-30} esu)	$ \mu\beta_{zzz} $ (10^{-48} esu)
E1	31.1	945	29 400	370 ± 10	11 500
E2a	52.1	2300	121 000	1520 ± 80	79 900
E2b	52.1	2860	148 000	1650 ± 150	86 000

value at 900 nm is 0.643×10^{-30} esu. And fourth, the HRS signal (squared), β_{HRS}^2 , is interpreted as coming from a single dipolar tensor component β_{zzz} as eqn (1) because the chromophores exhibit strong charge-transfer type electronic transitions, which is supported by theoretical computation, *vide infra*.

$$\langle \beta_{\text{HRS}}^2 \rangle = \langle \beta_{XZZ, \text{HRS}}^2 \rangle + \langle \beta_{ZZZ, \text{HRS}}^2 \rangle = \frac{6}{35} |\beta_{zzz}|^2 \quad (1)$$

where $\langle \beta_{\text{HRS}}^2 \rangle$ is the orientational averaged sum $\langle \beta_{XZZ, \text{HRS}}^2 \rangle$ and $\langle \beta_{ZZZ, \text{HRS}}^2 \rangle$ wherein the first subscript refers to the polarization state of the frequency doubled light, and the second and third subscripts refer to two Z-polarized laser photons. The X,Y,Z cartesian coordinates are as follows: X is the laser propagation

direction, Y is the direction towards the detector (*i.e.*, 90°), and Z is the laser polarization direction. Here, in uniaxial dipolar molecules, such as **E1** and **E2a-b**, the coordinates reduce to an expression within the molecular frame with z being the molecular dipolar axis.⁵⁴ The HRS values for beta are larger for **E2a-b**, which may, in part, stem from the greater charge separation as a result of the molecules being longer.

Computations

Quantum chemical calculations play an important role in predicting hyperpolarizability and dipole moment when designing new push-pull chromophores. DFT affords relatively high theory level for the large molecules studied in this work in comparison to semiempirical methods used in the past.³⁸ M06-2X exchange-correlation functional calculations predicts the static $|\beta|$ to be as high as 2860×10^{-30} esu for **E2b** with corresponding $\mu\beta$ of $148\,000 \times 10^{-48}$ esu followed by $|\beta|$ of 2300×10^{-30} esu and $\mu\beta$ $121\,000 \times 10^{-48}$ esu for **E2a**, and $|\beta|$ of 945×10^{-30} esu and $\mu\beta$ $29\,400 \times 10^{-48}$ esu for **E1**, Table 2. DFT calculations often overestimate β in comparison to experimental determination by as much as 2–3 times. Such is the case in the current study wherein the computed static absolute $|\beta|$ values in vacuum are a factor of 1.5 to 2.5 greater than the experimental HRS measurements at 900 nm in MeCN. A contributing factor to this difference is self-interaction error. Kohn–Sham DFT description of the electronic structure tends to overdelocalize the electrons (and hence overestimate both μ and $|\beta|$). This issue is partially mitigated by using hybrid exchange-correlation functionals with a larger fraction of exact Hartree–Fock (HF) exchange. In this case, M06-2X is a global hybrid functional with 54% HF exchange.

Computed HOMO and LUMO spatial distributions for **E1** and **E2a-b** demonstrate that the HOMO primarily localizes on the dicyanomethanide substituent while the LUMO localizes on the pyridinium cation, Fig. 4. One can observe a greater level of electron localization for compound **E2a-b** than compound **E1** due to the increase in π -system length. Addition of the phenylene ring adjacent to the dicyanomethanide in **E2a-b** causes a significant increase in optical excitation energy, ΔE , from

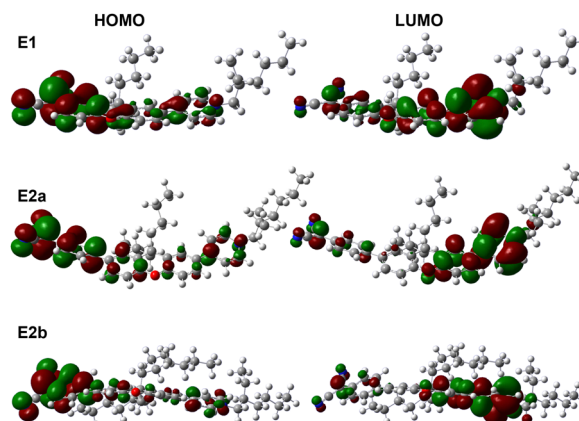


Fig. 4 Computed HOMO-LUMO for **E1** and **E2a-b** chromophores.



2.40 eV for **E1** to 2.96 eV for both **E2a** and **E2b**, Table 2. The predictions of absorption wavelength (and corresponding optical excitation energy values) are made possible *via* TD-DFT calculations using the M05-QX exchange-correlation functional derived by interpolation between M05 and M05-2X functionals.^{40,41} The values of dipole moment, μ , also increase with the length of the molecule from 31.1 *Debye* for **E1** to 52.5 *Debye* and 52.1 *Debye* for **E2a** and **E2b**, respectively, Table 1. The computed dihedral twist angle between the pyridinium ring and the xanthene bridge is 11.6° for **E1** and increases to 16.8° and 17.4°, respectively for **E2a** and **E2b**. The phenylene ring positioned between the electron donating dicyanomethanide and the planar xanthene bridge in **E2a-b** results in an additional twist angle which, when computed, increases from 25.6° for **E2a** to 35° for **E2b**. The nearly 10° increase in computed, out-of-plane rotation is likely due to the increase in sterics stemming from the bulkier ethyl-hexyl substituents in comparison to the less bulky butyl substituents on **E2a**, Table 1. A significant observation is that the dihedral angles for **E1** and **E2a-b** are low in comparison to other TICT chromophores with similar $|\mu\beta|$, which exhibit angles exceeding 65°. Thus, future derivatives of structurally modular **E1** and **E2a-b** with larger dihedral angles originating from bulkier substituents are likely to yield much higher $|\beta|$.

Electrochemical analysis

Fig. S34–S36 (ESI†) provide representative cyclic voltammograms (CV) for **E1** and **E2a-b**. The CVs have similar shape for each chromophore with a reductive peak near -1.75 V and a pair of oxidative peaks just above and below 0.5 V (*vs.* $\text{FeCp}_2^+/\text{FeCp}_2$ taken at 0 V). An additional unidentified peak exists near 0 V for each chromophore. Changing the concentration and the scan rate does not alter the magnitude of the peak current relative to the other signals ruling out contribution from aggregation. The CV features are reoccurring and remain constant over multiple scans. Alternative solvents, THF and DMF, were evaluated; however, the results were inconclusive possibly because the peaks were outside the electrochemical signal range of the solvents. There is an additional small wave at *ca.* -1.5 V, which is unidentified but may originate from the electrolyte. Further, when comparing the HOMO–LUMO gaps to the distances between the reductive wave and the unidentified peaks, the calculated result corresponds to wavelengths of light in the near IR regions. However, the calculations do not correspond to experimental or computational observations and are thus unsuitable to consider. Instead, calculation of the electrochemical band gaps using the designated reductive peak and the first oxidative peak, yields respective **E1**, **E2a**, and **E2b** values of 1.99 eV, 2.06 eV, 2.03 eV. These values are somewhat consistent with the estimated optical band gaps in MeCN, 2.05 eV, 2.37 eV, 2.33 eV, but differ greatly with the computed band gaps, 2.40 eV, 2.96 eV, and 2.96 eV for **E1**, **E2a**, and **E2b**, respectively, Table 1. The value disparity between methods is likely due to the complicated nature of the compounds being analyzed, where solvatochromatic and aggregation effects often cause deviations from predictive behavior.

Electro optic (EO) coefficient

Despite the large hyperpolarizability values observed both experimentally with HRS and computationally with DFT, the average r_{33} EO coefficient for ITO-EOP-Au device stacks is 0.93 pm V^{-1} and 1.3 pm V^{-1} for **E1** and **E2a**, respectively. **E2b** was not evaluated due to facility access limitations but is likely to yield similar r_{33} to **E1** and **E2a**. The chromophores were first poled using thermally assisted electric poling at 25 $\text{V } \mu\text{m}^{-1}$ at 110 °C. Larger voltages lead to dielectric breakdown, likely due to the thin nature of the EOP films (≤ 1 μm). The 110 °C poling temperature was selected based on the glass transition temperature of 5 wt% chromophore in poly(vinyl phenol) (PVP), Fig. S32–S33 (ESI†). The negligible EO coefficients may stem from low chromophore wt.% concentration, *in situ* degradation, or weak interactions between the chromophore and the polymer host. Low wt% concentrations were used due to aggregation concerns, as has been observed with other TICT chromophores.¹⁶ Difficulties encountered during filtration (0.2 μm PTFE syringe filter) may have further reduced the final wt% concentration thereby further thwarting the EO effect. The possibility of degradation was minimized by avoiding light and using low moisture nitrogen atmospheres during poling and r_{33} measurements; however, due to the limited air stability particularly for **E1**, some degradation could have occurred during the multi-step characterization process. Poor intermolecular interaction between chromophores and polymer hosts is a common challenge in producing EO polymer composites. The zwitterionic nature of the chromophores under investigation in the present work likely exacerbates the limited chromophore-polymer compatibility. To facilitate chromophore dispersion we used PVP as the polymer host in place of traditional polycarbonate (PC) or poly(methyl methacrylate) based on previous success with observing an increased EO effect with PVP, instead of PC, as a host for TICT chromophores.¹⁶ In the present work, however, the strength of aggregation likely exceeds the external electric field forces that would otherwise induce angular rotation about the chromophore's long, *Z*-axis enabling non-centrosymmetric head-to-head alignment during poling. The strong aggregation may be attributed to the narrow chromophore shape and large dipole moments in addition to their zwitterionic structure.

Conclusions

We report here a new class of π -conjugated, zwitterionic chromophores that, despite having low out-of-plane dihedral angles determined by simulation, exhibit large $|\beta|$ values ranging from $370 \pm 10 \times 10^{-30}$ esu to $1650 \pm 150 \times 10^{-30}$ esu, observed by HRS in MeCN at 900 nm. A further unique attribute of the push-pull chromophores is the xanthene bridge connecting the dicyanomethanide electron donor and alkyl pyridinium electron acceptor moieties, which simultaneously allows for the easy exchange of aliphatic substituents and increases β by way of greater charge localization. The compounds show positive correlations with π -system length, extent of aliphatic character,



and out-of-plane dihedral twist angles. Chromophore design was facilitated by computational efforts in predicting large absolute $|\beta|$ values prior to experimental synthesis. The chromophores were prepared using straightforward synthetic techniques and characterized using a battery of methods. While our computational model predicted higher absolute $|\beta|$ values (from 945×10^{-30} esu to 2860×10^{-30} esu) in comparison to experimental HRS characterization, the difference is expected due to the tendency of the overdelocalization of electrons in self-interacting DFT. The use of hybrid exchange-correlation functionals with a larger fraction of HF exchange partially mitigates this overdelocalization. Chromophore stability is greatest for **E2b**, which features relative stability for up to a week, followed by **E2a** which shows only slight degradation at 72 h, with **E1** showing moderate degradation over the same period. The r_{33} for **E1** and **E2a** were $\leq 1.3 \text{ pm V}^{-1}$ (not measured for **E2b**) likely due to strong aggregation of their π -conjugated, zwitterionic structures. However, we believe this difficulty to be surmountable given the wide synthetic latitude available in the form of incorporating aliphatic groups, increasing dihedral angles, as well as methods to increase productive guest–host interactions *via* covalent or intermolecular interactions. These research avenues are under development in our lab and will be disseminated in due course.

Author contributions

G. S. P.: chromophore design, synthesis, characterization, and manuscript write-up; Y. d. C. and K. C.: HRS measurements; A. E. M.: chromophore characterization; M. W. and A. E. M.: DFT calculations; K. E. C.: chromophore design, project management, manuscript write-up. The manuscript was written through contributions of all authors. All authors have given approval to the final version of the manuscript.

Conflicts of interest

There are no conflicts to declare.

Acknowledgements

G. S. P. acknowledges the P3 Postdoctoral Fellowship support through the University of Central Florida (UCF). Y. d. C. acknowledges a postdoctoral fellowship from FWO-V (Fonds Wetenschappelijk Onderzoek; number 1234222N), the Flemish Fund for Scientific Research. K. E. C. and G. S. P. acknowledge funding provided by the University of Central Florida and the kind collaboration with Prof. Fernando Uribe-Romo for enabling use of his research facilities. A. E. M. acknowledges support by the “improving of the competitiveness” program of the National Research Nuclear University MEPhI. This work used the Extreme Science and Engineering Discovery Environment (XSEDE), which is supported by National Science Foundation grant number ACI-1548562. The authors acknowledge the use of the following resources that have contributed to the

research results reported within this paper: Stampede2 facility of the Texas Advanced Computing Center (TACC) at The University of Texas at Austin (<https://www.tacc.utexas.edu>), the Stokes facility at the University of Central Florida Advanced Research Computing Center (<https://www.arcc.ist.ucf.edu>) and TORNADO facility at South Ural State University (<https://www.supercomputer.susu.ru>).

References

- 1 L. Beverina and G. A. Pagani, *Acc. Chem. Res.*, 2014, **47**, 319–329.
- 2 T. Sakamoto, T. Kawanishi and M. Tsuchiya, *Opt. Lett.*, 2008, **33**, 890–892.
- 3 L. Bai, Z. Lin, Z. Wang, C. Chen and M.-H. Lee, *J. Chem. Phys.*, 2004, **120**, 8772–8778.
- 4 W. Denk, H. Strickler James and W. Webb Watt, *Science*, 1990, **248**, 73–76.
- 5 J.-X. Cheng and X. S. Xie, *Science*, 2015, **350**, aaa8870.
- 6 A. Guillén-López, C. Delesma, C. Amador-Bedolla, M. Robles and J. Muñoz, *Theor. Chem. Acc.*, 2018, **137**, 85.
- 7 I.-C. Benea-Chelmus, M. L. Meretska, D. L. Elder, M. Tamagnone, L. R. Dalton and F. Capasso, *Nat. Commun.*, 2021, **12**, 5928.
- 8 J. Liu, C. Ouyang, F. Huo, W. He and A. Cao, *Dyes Pigm.*, 2020, **181**, 108509.
- 9 Y. Shi, D. Frattarelli, N. Watanabe, A. Facchetti, E. Cariati, S. Righetto, E. Tordin, C. Zuccaccia, A. Macchioni, S. L. Wegener, C. L. Stern, M. A. Ratner and T. J. Marks, *J. Am. Chem. Soc.*, 2015, **137**, 12521–12538.
- 10 R. Andreu, E. Galán, J. Garín, V. Herrero, E. Lacarra, J. Orduna, R. Alicante and B. Villacampa, *J. Org. Chem.*, 2010, **75**, 1684–1692.
- 11 A. J.-T. Lou and T. J. Marks, *Acc. Chem. Res.*, 2019, **52**, 1428–1438.
- 12 L. Dalton, A. Harper, A. Ren, F. Wang, G. Todorova, J. Chen, C. Zhang and M. Lee, *Ind. Eng. Chem. Res.*, 1999, **38**, 8–33.
- 13 H. Xu, F. Liu, D. L. Elder, L. E. Johnson, Y. De Coene, K. Clays, B. H. Robinson and L. R. Dalton, *Chem. Mater.*, 2020, **32**, 1408–1421.
- 14 I. D. L. Albert, T. J. Marks and M. A. Ratner, *J. Am. Chem. Soc.*, 1998, **120**, 11174–11181.
- 15 I. D. L. Albert, T. J. Marks and M. A. Ratner, *J. Am. Chem. Soc.*, 1997, **119**, 3155–3156.
- 16 H. Kang, A. Facchetti, P. Zhu, H. Jiang, Y. Yang, E. Cariati, S. Righetto, R. Ugo, C. Zuccaccia, A. Macchioni, C. L. Stern, Z. Liu, S.-T. Ho and T. J. Marks, *Angew. Chem., Int. Ed.*, 2005, **44**, 7922–7925.
- 17 M. R. Leahy-Hoppa, P. D. Cunningham, J. A. French and L. M. Hayden, *J. Phys. Chem. A*, 2006, **110**, 5792–5797.
- 18 A. M. R. Beaudin, N. Song, Y. Bai, L. Men, J. P. Gao, Z. Y. Wang, M. Szablewski, G. Cross, W. Wenseleers, J. Campo and E. Goovaerts, *Chem. Mater.*, 2006, **18**, 1079–1084.
- 19 Y. Wang, D. L. Frattarelli, A. Facchetti, E. Cariati, E. Tordin, R. Ugo, C. Zuccaccia, A. Macchioni, S. L. Wegener,



- C. L. Stern, M. A. Ratner and T. J. Marks, *J. Phys. Chem. C*, 2008, **112**, 8005–8015.
- 20 H. Kang, A. Facchetti, H. Jiang, E. Cariati, S. Righetto, R. Ugo, C. Zuccaccia, A. Macchioni, C. L. Stern, Z. Liu, S.-T. Ho, E. C. Brown, M. A. Ratner and T. J. Marks, *J. Am. Chem. Soc.*, 2007, **129**, 3267–3286.
- 21 G. S. He, J. Zhu, A. Baev, M. Samoć, D. L. Frattarelli, N. Watanabe, A. Facchetti, H. Ågren, T. J. Marks and P. N. Prasad, *J. Am. Chem. Soc.*, 2011, **133**, 6675–6680.
- 22 D. J. Clarke, A. Middleton, A. Teshome, M. D. H. Bhuiyan, M. Ashraf, G. J. Gainsford, I. Asselberghs, K. Clays, G. J. Smith and A. J. Kay, *AIP Conf. Proc.*, 2009, **1151**, 90.
- 23 S. Ito, S. Hiroto, S. Lee, M. Son, I. Hisaki, T. Yoshida, D. Kim, N. Kobayashi and H. Shinokubo, *J. Am. Chem. Soc.*, 2015, **137**, 142–145.
- 24 N. B. Teran, G. S. He, A. Baev, Y. Shi, M. T. Swihart, P. N. Prasad, T. J. Marks and J. R. Reynolds, *J. Am. Chem. Soc.*, 2016, **138**, 6975–6984.
- 25 A. J.-T. Lou, S. Righetto, C. Barger, C. Zuccaccia, E. Cariati, A. Macchioni and T. J. Marks, *J. Am. Chem. Soc.*, 2018, **140**, 8746–8755.
- 26 J. Xu, A. Takai, A. Bannaron, T. Nakagawa, Y. Matsuo, M. Sugimoto, Y. Matsushita and M. Takeuchi, *Mater. Chem. Front.*, 2018, **2**, 780–784.
- 27 J. Jia, X. Wu, Y. Fang, J. Yang, Y. Han, J. Xiao, X. Zhang, Y. Wang and Y. Song, *J. Phys. Chem. C*, 2020, **124**, 4701–4708.
- 28 X. Chen, T. Pradhan, F. Wang, J. S. Kim and J. Yoon, *Chem. Rev.*, 2012, **112**, 1910–1956.
- 29 A. Abboto, *Gazz. Chim. Ital.*, 1997, **127**, 165–166.
- 30 F. Meyers, S. R. Marder, B. M. Pierce and J. L. Bredas, *J. Am. Chem. Soc.*, 1994, **116**, 10703–10714.
- 31 A. C. Spivey, L. Shukla and J. F. Hayler, *Org. Lett.*, 2007, **9**, 891–894.
- 32 Y. Ashikari, T. Kawaguchi, K. Mandai, Y. Aizawa and A. Nagaki, *J. Am. Chem. Soc.*, 2020, **142**, 17039–17047.
- 33 Y. Morisaki, T. Nakano and Y. Chujo, *J. Polym. Sci., Part A: Polym. Chem.*, 2014, **52**, 2815–2821.
- 34 J. Campo, F. Desmet, W. Wenseleers and E. Goovaerts, *Opt. Express*, 2009, **17**, 4587–4604.
- 35 Y. De Coene, O. Deschaume, S. Jooen, S. Seré, S. Van Cleuvenbergen, C. Bartic, T. Verbiest and K. Clays, *Chem. Mater.*, 2020, **32**, 7327–7337.
- 36 M. J. Frisch, G. W. Trucks, H. B. Schlegel, G. E. Scuseria, M. A. Robb, J. R. Cheeseman, G. Scalmani, V. Barone, B. Mennucci, G. A. Petersson, H. Nakatsuji, M. Caricato, X. Li, H. P. Hratchian, A. F. Izmaylov, J. Bloino, G. Zheng, J. L. Sonnenberg, M. Hada, M. Ehara, K. Toyota, R. Fukuda, J. Hasegawa, M. Ishida, T. Nakajima, Y. Honda, O. Kitao, H. Nakai, T. Vreven, J. J. A. Montgomery, J. E. Peralta, F. Ogliaro, M. Bearpark, J. J. Heyd, E. Brothers, K. N. Kudin, V. N. Staroverov, R. Kobayashi, J. Normand, K. Raghavachari, A. Rendell, J. C. Burant, S. S. Iyengar, J. Tomasi, M. Cossi, N. Rega, N. J. Millam, M. Klene, J. E. Knox, J. B. Cross, V. Bakken, C. Adamo, J. Jaramillo, R. Gomperts, R. E. Stratmann, O. Yazyev, A. J. Austin, R. Cammi, C. Pomelli, J. W. Ochterski, R. L. Martin, K. Morokuma, V. G. Zakrzewski, G. A. Voth, P. Salvador, J. J. Dannenberg, S. Dapprich, A. D. Daniels, Ö. Farkas, J. B. Foresman, J. V. Ortiz, J. Cioslowski and D. J. Fox, *Gaussian 09, Revision D.01*, 2009, 1639769047.
- 37 T. H. Dunning Jr. and P. J. Hay, in *Methods of Electronic Structure Theory*, ed., H. F. Schaefer III, Springer, New York, 1977, vol. 3, pp. 1–27.
- 38 L. E. Johnson, L. R. Dalton and B. H. Robinson, *Acc. Chem. Res.*, 2014, **47**, 3258–3265.
- 39 A. V. Marenich, C. J. Cramer and D. G. Truhlar, *J. Phys. Chem. B*, 2009, **113**, 6378–6396.
- 40 I. A. Mikhailov, M. V. Bondar, K. D. Belfield and A. E. Masunov, *J. Phys. Chem. C*, 2009, **113**, 20719–20724.
- 41 Y. Zhao, N. E. Schultz and D. G. Truhlar, *J. Chem. Theory Comput.*, 2006, **2**, 364–382.
- 42 K. Y. Suponitsky, S. Tafur and A. E. Masunov, *J. Chem. Phys.*, 2008, **129**, 044109.
- 43 K. Y. Suponitsky, A. E. Masunov and M. Y. Antipin, *Mendeleev Commun.*, 2008, **18**, 265–267.
- 44 K. Y. Suponitsky, Y. Liao and A. E. Masunov, *J. Phys. Chem. A*, 2009, **113**, 10994–11001.
- 45 K. Y. Suponitsky, A. E. Masunov and M. Y. Antipin, *Mendeleev Commun.*, 2009, **19**, 311–313.
- 46 K. Y. Suponitsky and A. E. Masunov, *J. Chem. Phys.*, 2013, **139**, 094310.
- 47 L. Croitor, E. B. Coropceanu, A. V. Siminel, A. E. Masunov and M. S. Fonari, *Polyhedron*, 2013, **60**, 140–150.
- 48 Y. O. Shaydyuk, S. M. Levchenko, S. A. Kurhuzenkau, D. Anderson, A. E. Masunov, O. D. Kachkovsky, Y. L. Slominsky, J. L. Bricks, K. D. Belfield and M. V. Bondar, *J. Lumin.*, 2017, **183**, 360–367.
- 49 W. V. Moreshead, O. V. Przhonska, M. V. Bondar, A. D. Kachkovski, I. H. Nayyar, A. E. Masunov, A. W. Woodward and K. D. Belfield, *J. Phys. Chem. C*, 2013, **117**, 23133–23147.
- 50 B. Sui, M. V. Bondar, D. Anderson, H. J. Rivera-Jacquez, A. E. Masunov and K. D. Belfield, *J. Phys. Chem. C*, 2016, **120**, 14317–14329.
- 51 I. H. Nayyar, A. E. Masunov and S. Tretiak, *J. Phys. Chem. C*, 2013, **117**, 18170–18189.
- 52 I. A. Mikhailov, M. Musiał and A. E. Masunov, *Comput. Theor. Chem.*, 2013, **1019**, 23–32.
- 53 A. J.-T. Lou and T. J. Marks, *Acc. Chem. Res.*, 2019, **52**, 1428–1438.
- 54 Y. de Coene, S. Van Cleuvenbergen, N. Van Steerteghem, V. Baekelandt, T. Verbiest, C. Bartic and K. Clays, *J. Phys. Chem. C*, 2017, **121**, 6909–6915.

